Energetic study of the transition to nonlinear state in two-dimensional electron temperature gradient fluid turbulence

J.-H. Kim[a] and P. W. Terry
Department of Physics, University of Wisconsin at Madison, Madison, Wisconsin 53706, USA

(Received 6 July 2010; accepted 14 September 2010; published online 9 November 2010)

Eigenmode projection has been used in analysis of the two-dimensional numerical solution of electron temperature gradient (ETG) turbulence. The secondary Kelvin–Helmholtz instability (KHI) that breaks up the primary ETG structure at the onset of saturation is found to be associated with strong excitation of damped eigenmodes and strong energy damping. While the KHI structure induces some fine scale motions, which can be dissipated by collisional damping, the structure also damps directly at low poloidal wavenumbers through stable eigenmodes. The latter process is persistent in time, while the former occurs only transiently at the initial breakdown of the linearly dominant ETG structure. The persistence of energy damping by stable eigenmodes during and after the transition is enabled by nonlinear advection of electron pressure. Thus, KHI in this system couples with electron pressure advection to generate a dissipative structure at low poloidal wavenumber. © *2010 American Institute of Physics*. [doi:10.1063/1.3496394]

I. INTRODUCTION

Plasma microinstabilities saturate by nonlinear energy transfer to dissipative structures. Because plasma nonlinearities couple different scales, dissipative structures are usually thought of as a set of scales away from those of the instability. Saturation, in analogy with the hydrodynamic cascade, is then a matter of energy transfer across scales, from those of the instability to those of dissipation. In years past, when plasma turbulence was viewed more as a process of nonlinear wave interaction than a cascade, a second type of saturation mechanism was invoked. This involved the postulate that the nonlinearity coupled the unstable mode to a second specified collective mode that was damped, and therefore able to provide saturation. In this type of exercise, the damped mode was hand picked from established linear collective plasma modes and its dispersive properties were treated in the saturation analysis. This view has fallen out of favor as a picture of plasma turbulence has been sought that is less tied to linear modes and more universal.

However, efforts at understanding the saturation of instabilities believed to govern transport losses in fusion plasmas have brought damped eigenmodes back into the picture.[1–5] The damped eigenmodes are not necessarily special or identifiable from the literature of collective modes. Rather, they are whatever linear roots arise in the system of equations used to model an instability. These roots need not all be damped, but generally there is at least one, and in some cases many, that are damped for all wavenumbers. All such roots are pumped by the three-wave coupling of the nonlinearity. Their final amplitude in the steady state, and hence their importance in saturation of the instability, depends on their linear damping rate and the strength of nonlinear coupling. Nonlinear excitation of stable eigenmodes has been shown to govern saturation in the two-field fluid model for collisionless trapped electron mode turbulence,[1] the three-field fluid model for ion temperature gradient (ITG) driven mode turbulence,[2] and ITG gyrokinetic turbulence.[5] In gyrokinetics the number of distinct damped eigenmodes excited is so large that elements of universality are evident in the saturated state.[5] Nonlinearly excited damped eigenmodes have also been recognized to affect the cross phase of transport fluxes, including particle,[3] momentum,[6] and heat flux.[5]

This paper explores the transition from the linear growth phase to the nonlinear phase of electron temperature gradient (ETG) turbulence. It examines fluctuation energy transfer among unstable and stable modes, and an equilibrium. The term "*damped mode*" is used interchangeably with "*stable mode*," but we are particularly interested in modes that provide an energy damping mechanism. The paper deals with two questions. The first is whether the Kelvin–Helmholtz instability (KHI) provides a largely conservative route to small scale dissipation, or whether it creates dissipative structure at its largest scales through damped eigenmodes. The KHI is a secondary instability associated with a finite-amplitude electric potential structure, and is the main mechanism for the transition from a linear regime to a nonlinear regime in turbulence driven by the ETG instability.[7,8] Here we define KHI loosely by the nonlinear action of $\boldsymbol{E}\times\boldsymbol{B}$ advection of the electron polarization density $\boldsymbol{v}_E\cdot\nabla\nabla^2\phi$. As later recognized, this is consistent with the standard definition.[7,9] It has been assumed that the KHI transfers energy conservatively to large wavenumber k where it is dissipated. The second question asks which aspects of the secondary KHI and damped eigenmode excitation are persistent features of the saturation of the primary ETG instability, or merely transients. Noting that descriptions of the saturation of the ETG instability have invoked a tertiary instability,[7,10] this question ultimately deals with whether the analysis of the excitation of damped eigenmodes describes long-time properties of the saturated state. These questions are investi-

[a]Electronic mail: jkim282@wisc.edu.

gated numerically with a two-dimensional (2D) reduced fluid model of the ETG mode.

Due to the possibility of significant excitation of damped modes, the energy dynamics of KHI might be expected to be more complex than assumed previously. Because they have a dissipative structure even at low poloidal wavenumber, the damped modes may be large enough to dissipate the fluctuation energy at a rate that is comparable to high-k dissipation. To investigate this possibility, detailed examination of the energy dynamics is required. The energy dynamics is analyzed at each wavenumber and separated into contributions associated with unstable and stable eigenmodes, allowing determination of the relative partition. The rates at which energy is injected into the turbulence, transferred, and removed from the turbulence are also tracked. Accounting for the energy dynamics among eigenmodes at each wavenumber gives a complicated but more complete picture of ETG saturation. The picture includes the roles of $\boldsymbol{E}\times\boldsymbol{B}$ advection of vorticity and electron pressure fluctuations during the transition. It should be noted that the word "dissipation" in the paper refers to energy damping of fluctuations, including both the cross-correlation, which gives rise to instability (stability) and sustains waves, and collisional damping, which produces irreversible dissipation in the thermodynamic sense. The relative contributions of collisional diffusivities and cross-correlations will be described toward the end of the paper.

The remainder of the paper is organized as follows. Our simulation model and method are described in Sec. II The energy equations are constructed and the energy transfer rates and growth rates, the main tools for our analysis, are defined and described in Sec. III. The detailed analysis of the role of damped modes is given in Sec. IV. The obtained results are summarized in Sec. V. Full mathematical expressions for the energetics analysis are given in the Appendix.

II. MODEL AND SIMULATION

In the sheared slab configuration, the equilibrium magnetic field is

$$\boldsymbol{B}=B_0\mathbf{b}_0=\boldsymbol{B}_0\left(\hat{z}+\frac{x-x_0}{L_s}\hat{\boldsymbol{y}}\right), \tag{1}$$

where $L_s=q(\mathrm{d}q/\mathrm{d}r)^{-1}$ is the magnetic shear gradient length. The derivative along a field line has the contribution from the background and perturbed magnetic field in the form

$$\hat{\boldsymbol{b}}\cdot\boldsymbol{\nabla}\xi=\left(\hat{\boldsymbol{b}}_0+\frac{\nabla\times A\hat{\boldsymbol{z}}}{B_0}\right)\cdot\boldsymbol{\nabla}\xi=\nabla_{||}\xi-\frac{1}{B_0}[A,\xi],$$

where

$$\nabla_{||}f=\left(\frac{\partial}{\partial z}+\frac{x-x_0}{L_s}\frac{\partial}{\partial y}\right)f \quad\text{and}\quad [f,g]=\frac{\partial f}{\partial x}\frac{\partial g}{\partial y}-\frac{\partial f}{\partial y}\frac{\partial g}{\partial x}. \tag{2}$$

Advection by the $\boldsymbol{E}\times\boldsymbol{B}$ velocity is given by

$$\boldsymbol{v}_{\boldsymbol{E}}\cdot\boldsymbol{\nabla}\xi=[\phi,\xi]. \tag{3}$$

Using the notation of Eqs. (2) and (3), the electromagnetic ETG model[8,11,12] is

$$(\tau-\nabla_\perp^2)\frac{\partial\phi}{\partial t}=[1-\epsilon_n+(1+\eta_e)\nabla_\perp^2]\frac{\partial\phi}{\partial y}+\nabla_\parallel\nabla_\perp^2A+\epsilon_n\frac{\partial p}{\partial y}+[\phi,\nabla_\perp^2\phi]-\frac{\beta_e}{2}[A,\nabla_\perp^2A]+\mu\nabla_\perp^2\nabla_\perp^2\phi, \tag{4a}$$

$$\left(\frac{\beta_e}{2}-\nabla_\perp^2\right)\frac{\partial A}{\partial t}=-\nabla_\parallel(\phi-p_e)-\frac{\beta_e}{2}(1+\eta_e)\frac{\partial A}{\partial y}+[\phi,\nabla_\perp^2A]-\frac{\beta_e}{2}[A,\phi-p]-\eta_{hv}\nabla_\perp^2\nabla_\perp^2\psi, \tag{4b}$$

$$\frac{\partial p}{\partial t}=-[1+\eta_e-\epsilon_n\Gamma(1-\tau)]\frac{\partial\phi}{\partial y}-\Gamma\nabla_\perp^2\frac{\partial A}{\partial z}-2\Gamma\epsilon_n\frac{\partial p}{\partial y}-[\phi,p]+\Gamma\frac{\beta_e}{2}[A,\nabla_\perp^2A]+\chi\nabla_\perp^2p, \tag{4c}$$

where $\eta_e=L_{ne}/L_{Te}$ is the ratio of the gradient lengths, $L_{n,T}$ and R are the gradient lengths of electron density, temperature, and toroidal magnetic field, and $\epsilon_n=L_n/R$ is the ratio of the diamagnetic drift frequency to the magnetic drift frequency. The electron plasma beta β_e is the ratio of the electron thermal pressure to the magnetic pressure. Also, note that (x,y) is normalized by the electron gyroradius $\rho_e=(m_eT_e)^{1/2}/eB$, z by the density gradient length L_n, and time t by L_n/v_{Te}, where $v_{Te}=(T_e/m_e)^{1/2}$ is the electron thermal velocity. The model includes the collisional diffusivities (hyperdiffusivities) for electrostatic, magnetic, and pressure fields. The coefficients are set to $O(1)$ in the following simulations. In the following equations, the collisional diffusivities may be not displayed, but all analyses, both nonlinear simulations and eigenmode calculations, include them. The fluctuations $(\hat{\phi},\hat{A},\delta\hat{p})$ are normalized as follows:

$$\frac{\rho_e}{L_n}\hat{\phi}\equiv\frac{e\phi}{T_e},\quad \frac{\rho_e}{L_n}\hat{A}\equiv\beta_e\frac{ev_{Te}A}{T_e},\quad\text{and}\quad \frac{\rho_e}{L_n}\delta\hat{p}\equiv\frac{\delta p_e}{p_e}. \tag{5}$$

The model describes the ETG mode at the electron gyroradius scale $k\rho_e^{-1}\sim1$ in the high density limit, $k_\perp\lambda_{de}\ll1$. Finite Larmor radius (FLR) effects are included as first-order corrections and FLR stabilization is approximated in the viscous term. The model has the curvature effect and electron compression from the toroidicity.

From Eqs. (4a)–(4c), the energy evolution for each field is given by

$$\frac{\mathrm{dE}_\phi}{\mathrm{d}t}=\langle\phi\nabla_\parallel\nabla_\perp^2A\rangle+\epsilon_n\left\langle\phi\frac{\partial p}{\partial y}\right\rangle-\frac{\beta}{2}\langle\phi[A,\nabla_\perp^2A]\rangle+\left.\frac{\mathrm{dE}_\phi}{\mathrm{d}t}\right|_D, \tag{6a}$$

$$\frac{\mathrm{dE}_A}{\mathrm{d}t}=\langle\nabla_\parallel(\phi-p)\nabla_\perp^2A\rangle+\frac{\beta}{2}\langle\phi[A,\nabla^2A]\rangle-\frac{\beta}{2}\langle p[A,\nabla^2A]\rangle+\left.\frac{\mathrm{dE}_A}{\mathrm{d}t}\right|_D, \tag{6b}$$

$$\frac{dE_p}{dt} = -\left(\frac{1+\eta_e}{\Gamma} - \epsilon_n(1-\tau)\right)\left\langle p\frac{\partial\phi}{\partial y}\right\rangle - \langle p\nabla_\parallel\nabla_\perp^2 A\rangle + \frac{\beta}{2}\langle p[A,\nabla_\perp^2 A]\rangle + \left.\frac{dE_p}{dt}\right|_D, \tag{6c}$$

where

$$E_\phi = \tfrac{1}{2}\langle\tau|\phi|^2 + |\boldsymbol{\nabla}_\perp\phi|^2\rangle,$$

$$E_A = \frac{1}{2}\left\langle\frac{\beta}{2}|\boldsymbol{\nabla}_\perp A|^2 + |\nabla_\perp^2 A|^2\right\rangle, \tag{7}$$

$$E_p = \frac{1}{2\Gamma}\langle|p|^2\rangle,$$

and the $\langle\cdots\rangle$ brackets represent the spatial average and $d/dt|_D$ represents the decay rate of the collisional diffusivities. The quantity E_ϕ is the electrostatic potential energy and electron perpendicular kinetic energy, E_A is the electron parallel kinetic energy and magnetic field energy, and E_p is the electron pressure energy. The system is taken as periodic in the y domain. The total energy evolves according to

$$\frac{dE_{tot}}{dt} = \left(\frac{1+\eta_e}{\Gamma} + \epsilon_n\tau\right)\left\langle -p\frac{\partial\phi}{\partial y}\right\rangle + \left.\frac{dE_{tot}}{dt}\right|_D. \tag{8}$$

The quantity in brackets is the electrostatic thermal flux $q_e = \langle v_x p\rangle = \langle p(-\partial\phi/\partial y)\rangle$.

The model is implemented in the code as

$$\frac{\partial\Omega}{\partial t} - \mu\nabla_\perp^2\Omega = L_1(\phi,\Omega,A,J,p) + [\phi,\nabla_\perp^2\phi] + \frac{\beta_e}{2}[A,\nabla_\perp^2 A], \tag{9a}$$

$$\frac{\partial J}{\partial t} - \eta_{hv}\nabla_\perp^2 J = L_2(\phi,\Omega,A,J,p) + [\phi,\nabla_\perp^2 A] + [A,\phi-p], \tag{9b}$$

$$\frac{\partial p}{\partial t} - \chi_\perp\nabla_\perp^2 p = L_3(\phi,\Omega,A,J,p) - [\phi,p] + [A,\nabla_\perp^2 A], \tag{9c}$$

where $\Omega=(\tau-\nabla_\perp^2)\phi$ is the "effective vorticity" fluctuation, and $J=(\beta_e/2-\nabla_\perp^2)A$ is the "effective parallel current" fluctuation.

The simulation code is written with the Fourier–Chebyshev pseudospectral method,[13] with Gauss–Lobatto points $x_n/L_x=\cos(\pi n/N_x)$ where $n=0,1,\ldots,N_x$. With Chebyshev polynomials in the radial direction (x) and Fourier series in the poloidal (y), any field of ξ is expressible as

$$\xi(x,y) = \sum_{\ell mn}\xi_{\ell m}T_\ell\left(\frac{x}{L_x}\right)\exp\left(i\frac{2\pi m}{L_y}y\right), \tag{10}$$

where $T_\ell(x/L_x)$ is the ℓth-order Chebyshev polynomial and the domain of x is $[-L_x,L_x]$. The boundary conditions in the radial domain are

$$\phi(\pm L_x) = \Omega(\pm L_x) = A(\pm L_x) = J(\pm L_x) = p(\pm L_x) = 0.$$

The time integration of the fluctuation (Ω,J,p) is implemented with a third-order Adam–Bashford method (AB3) with the backward Euler method.[13] The diffusion-like terms $\mu\nabla_\perp^2\Omega$, $\eta_{hv}\nabla_\perp^2 J$, and $\chi_\perp\nabla_\perp^2 p$ are advanced implicitly with the backward Euler method, and the other linear and nonlinear terms are advanced explicitly with AB3.

Given $k_y=2\pi m/L_y$, the eigenvalue problem is written in the form

$$\lambda\begin{pmatrix}\bar{\bar{I}} & \bar{\bar{0}} & \bar{\bar{0}} & \bar{\bar{0}} & \bar{\bar{0}}\\ \bar{\bar{0}} & \bar{\bar{I}} & \bar{\bar{0}} & \bar{\bar{0}} & \bar{\bar{0}}\\ \bar{\bar{0}} & \bar{\bar{0}} & \bar{\bar{I}} & \bar{\bar{0}} & \bar{\bar{0}}\\ \bar{\bar{0}} & \bar{\bar{0}} & \bar{\bar{0}} & \bar{\bar{0}} & \bar{\bar{0}}\\ \bar{\bar{0}} & \bar{\bar{0}} & \bar{\bar{0}} & \bar{\bar{0}} & \bar{\bar{0}}\end{pmatrix}\begin{pmatrix}\bar{\Omega}\\ \bar{J}\\ \bar{p}\\ \bar{\phi}\\ \bar{A}\end{pmatrix} = \lambda\bar{\bar{M}}\begin{pmatrix}\bar{\Omega}\\ \bar{J}\\ \bar{p}\\ \bar{\phi}\\ \bar{A}\end{pmatrix} = \begin{pmatrix}\bar{\bar{L}}_{11} & \bar{\bar{L}}_{12} & \bar{\bar{L}}_{13} & \bar{\bar{L}}_{14} & \bar{\bar{L}}_{15}\\ \bar{\bar{L}}_{21} & \bar{\bar{L}}_{22} & \bar{\bar{L}}_{23} & \bar{\bar{L}}_{24} & \bar{\bar{L}}_{25}\\ \bar{\bar{L}}_{31} & \bar{\bar{L}}_{32} & \bar{\bar{L}}_{33} & \bar{\bar{L}}_{34} & \bar{\bar{L}}_{35}\\ -\bar{\bar{I}} & \bar{\bar{0}} & \bar{\bar{0}} & \bar{\bar{L}}_1 & \bar{\bar{0}}\\ \bar{\bar{0}} & -\bar{\bar{I}} & \bar{\bar{0}} & \bar{\bar{0}} & \bar{\bar{L}}_2\end{pmatrix}\begin{pmatrix}\bar{\Omega}\\ \bar{J}\\ \bar{p}\\ \bar{\phi}\\ \bar{A}\end{pmatrix} = \bar{\bar{L}}\begin{pmatrix}\bar{\Omega}\\ \bar{J}\\ \bar{p}\\ \bar{\phi}\\ \bar{A}\end{pmatrix}, \tag{11}$$

where $\bar{\bar{I}}$ is an identity matrix and the submatrices $\bar{\bar{L}}_{ij}$ and $\bar{\bar{L}}_i$ are of the second-order derivative.

Since the derivative of an nth order polynomial is of order $(n-1)$, the fields Ω and J are polynomials of order $(n-2)$. The total matrix size is $(5N_x+1)\times(5N_x+1)$. While the size of the matrix is larger than the size $(3N_x+3)\times(3N_x+3)$ of the original form in (ϕ,A,p), the norm $\|L\|_\infty\sim N_x^3$ of the current form gives better numerical results than the norm $\|L\|_\infty\sim N_x^7$ of the three-field form.[14] The two bottom rows are replaced with the corresponding boundary conditions $\bar{B}^\pm\cdot\bar{\xi}$. In addition, it must be noted that the left-hand side of the matrix is singular. The eigenvalue problem becomes a generalized eigenvalue problem $Ax=\lambda Bx$ with a singular matrix B. The QZ algorithm suitable for a generalized eigenvalue matrix is implemented with use of the relevant LAPACK subroutines. The code is parallelized on shared memory with GOTOBLAS2 (Ref. 15) supporting the OPENMP LAPACK library. The numerical accuracy of an eigenvector is checked by the convergence of the eigenvalues,[16] and the orthogonality of left and right eigenvectors.

The left and right eigenvectors $\bar{\eta}_i$ and $\bar{\zeta}_i$ for each eigenvalue λ_i satisfy

$$\bar{\bar{L}}\bar{\zeta}_i = \lambda_i\bar{\bar{M}}\bar{\zeta}_i, \quad \bar{\eta}_i^*\bar{\bar{L}} = \lambda_i\bar{\eta}_i^*\bar{\bar{M}}, \quad \text{and} \quad \bar{\eta}_i^*\bar{\bar{M}}\bar{\zeta}_j = \delta_{ij}, \tag{12}$$

where δ_{ij} is the Kronecker delta. The eigenvector $\bar{\eta}^*$ is the transposed, complex conjugate of the vector $\bar{\eta}$. Using $\bar{\zeta}_i$ and $\bar{\eta}_i$, a fluctuation $\bar{\zeta}$ is decomposed into the eigenmode basis,

$$\bar{\zeta} = \sum_i a_i \bar{\zeta}_i \quad \text{and} \quad a_i = \bar{\eta}_i^* \bar{\bar{M}} \bar{\zeta}. \tag{13}$$

III. FORMULATION OF ENERGETICS

In k space, the set of energy evolution equations is

$$\frac{dE_\phi(\boldsymbol{k})}{dt} = k_y \epsilon_n \,\mathrm{Im}\, p_{\boldsymbol{k}} \phi_{\boldsymbol{k}}^* - k_z k_\perp^2 \,\mathrm{Im}\, A_{\boldsymbol{k}} \phi_{\boldsymbol{k}}^* + \mathrm{Re}\left\{ \left([\phi, \nabla_\perp^2 \phi]_{\boldsymbol{k}} - \frac{\beta}{2} [A, \nabla_\perp^2 A]_{\boldsymbol{k}} \right) \phi_{\boldsymbol{k}}^* \right\}, \tag{14a}$$

$$\frac{dE_A(\boldsymbol{k})}{dt} = k_z k_\perp^2 \,\mathrm{Im}\{A_{\boldsymbol{k}} \phi_{\boldsymbol{k}}^* + A_{\boldsymbol{k}}^* p_{\boldsymbol{k}}\} + \mathrm{Re}\left\{ \left([\phi, \nabla_\perp^2 A]_{\boldsymbol{k}} - \frac{\beta}{2} [A, \phi - p]_{\boldsymbol{k}} \right) (-k_\perp^2 A_{\boldsymbol{k}}^*) \right\}, \tag{14b}$$

$$\frac{dE_p(\boldsymbol{k})}{dt} = k_y \left(\frac{1+\eta_e}{\Gamma} - \epsilon_n (1-\tau) \right) \mathrm{Im}\, p_{\boldsymbol{k}} \phi_{\boldsymbol{k}}^* - k_z k_\perp^2 \,\mathrm{Im}\, A_{\boldsymbol{k}}^* p_{\boldsymbol{k}} - \mathrm{Re}\left\{ \left(\frac{[\phi, p]_{\boldsymbol{k}}}{\Gamma} - \frac{\beta}{2} [A, \nabla_\perp^2 A]_{\boldsymbol{k}} \right) p_{\boldsymbol{k}}^* \right\}, \tag{14c}$$

where

$$E_\phi(\boldsymbol{k}) = \tfrac{1}{2}[(\tau + k_\perp^2)|\phi|^2],$$

$$E_A(\boldsymbol{k}) = \frac{1}{2}\left[\left(\frac{\beta}{2} + k_\perp^2 \right) k_\perp^2 |A|^2 \right],$$

and

$$E_p(\boldsymbol{k}) = \frac{1}{2}\left(\frac{|p|^2}{\Gamma} \right).$$

From Eqs. (14a)–(14c), the linear and nonlinear contributions to the rate of energy change can be distinguished according to

$$\frac{dE(\xi, \boldsymbol{k})}{dt} = \Gamma_T(\xi, \boldsymbol{k}) = \Gamma_L(\xi, \boldsymbol{k}) + \Gamma_N(\xi, \boldsymbol{k}), \tag{15}$$

where $\xi = \phi, A, p$, and the explicit expressions of $\Gamma_L(\xi, \boldsymbol{k})$ and $\Gamma_N(\xi, \boldsymbol{k})$ are given in Eqs. (A1)–(A3) of the Appendix. The linear and nonlinear energy transfer rates $\Gamma_L(\xi, \boldsymbol{k})$ and $\Gamma_N(\xi, \boldsymbol{k})$ are the contributions to the energy evolution by linear and nonlinear terms. It is noted that $\Gamma_N = \Sigma_{\xi, \boldsymbol{k}} \Gamma_N(\xi, \boldsymbol{k}) = 0$ in accordance with energy conservation.

The total, linear, and nonlinear energy transfer rates of a wavenumber $\boldsymbol{k}$ are the sum over the total, linear, and nonlinear contributions of each field, $\Gamma_{T,L,N}(\boldsymbol{k}) = \Sigma_\xi \Gamma_{T,L,N}(\xi; \boldsymbol{k})$. The "linear energy transfer rate" $\Gamma_L(\boldsymbol{k})$ is the quadratic contribution to the energy evolution in a wavenumber by the cross-correlation terms which give rise to drift instability and sustain linear drift waves, and the viscous damping terms which produce thermodynamic dissipation. At infinitesimal amplitude, $\Gamma_L(\xi, \boldsymbol{k}) = \gamma_0 E(\xi, \boldsymbol{k})$, where γ_0 is the linear growth rate of an eigenmode. At finite amplitude $\Gamma_L(\xi, \boldsymbol{k}) \neq \gamma_0 E(\xi, \boldsymbol{k})$, in general, because the cross phases of the correlations $\mathrm{Im}\, p_{\boldsymbol{k}} \phi_{\boldsymbol{k}}^*$, $\mathrm{Im}\, A_{\boldsymbol{k}} \phi_{\boldsymbol{k}}^*$, and $\mathrm{Im}\, A_{\boldsymbol{k}}^* p_{\boldsymbol{k}}$ that govern $\Gamma_L(\xi, \boldsymbol{k})$ are no longer determined solely by the most unstable eigenmode. Therefore, $\Gamma_L(\boldsymbol{k})$ is the finite-amplitude induced energy transfer rate between the wavenumber and the background. When $\Gamma_L(\boldsymbol{k}) > 0$ the energy is injected into wavenumber $\boldsymbol{k}$ by the amplitude-dependent growth rate from the energy available in the background gradient.

The "nonlinear energy transfer rate" $\Gamma_N(\boldsymbol{k})$ is the cubic contribution to the energy evolution at wavenumber $\boldsymbol{k}$ by nonlinear interaction among the wavenumbers. The condition $\Gamma_N > 0$ represents that the nonlinearity is transferring net energy into the wavenumber $\boldsymbol{k}$. The conservative nature of the nonlinear interactions gives $\Sigma_{\boldsymbol{k}} \Gamma_N(\boldsymbol{k}) = 0$, so that the nonlinear interactions redistribute the energy among the wavenumbers. The "total energy transfer rate" $\Gamma_T(\boldsymbol{k}) = \Gamma_L(\boldsymbol{k}) + \Gamma_N(\boldsymbol{k})$ is the total rate of the energy change of a wavenumber. The total energy transfer rate of a fluctuation at the wavenumber $\boldsymbol{k}$ that is increasing in time is positive whether it is unstable ($\Gamma_L(\boldsymbol{k}) > 0$) or receiving net energy from nonlinear transfer ($\Gamma_N(\boldsymbol{k}) > 0$). For the whole system of fluctuations, $\Sigma_{\boldsymbol{k}} \Gamma_T(\boldsymbol{k}) = \Sigma_{\boldsymbol{k}} \Gamma_L(\boldsymbol{k})$ is valid since $\Sigma_{\boldsymbol{k}} \Gamma_N(\boldsymbol{k}) = 0$.

Growth rates with units of t^{-1} are defined as

$$\gamma_i(\xi, \boldsymbol{k}) = \frac{\Gamma_i(\xi, \boldsymbol{k})}{2E_{\boldsymbol{k}}}, \quad \gamma_i(\boldsymbol{k}) = \sum_\xi \gamma_i(\xi, \boldsymbol{k}), \quad \text{and} \quad \gamma_i = \frac{1}{E_{\mathrm{tot}}} \sum_{\xi, \boldsymbol{k}} \Gamma_i(\xi, \boldsymbol{k}), \tag{16}$$

where $i = T, L, N$. As discussed above, the total, linear, and nonlinear growth rates $\gamma_{T,L,N}$ are different from the linear growth rate γ_0 of an eigenmode. The definitions give that $\gamma_T(k_0) = \gamma_L(k_0) = \gamma_0$ when the most unstable mode of the wavenumber k_0 is dominant in the linear phase and the linear growth rate of the mode is γ_0.

The meaning of each growth rate can be illustrated by Kolmogorov-type steady turbulence. In the steady state, the total growth rates at the energy injection scale $k = k_1$ and the energy dissipation scale $k = k_2$ are statistically zero and

$$\gamma_T(k_1) = 0 = \gamma_L(k_1) + \gamma_N(k_1), \Rightarrow \gamma_L(k_1) = -\gamma_N(k_1) > 0,$$

$$\gamma_T(k_2) = 0 = \gamma_L(k_2) + \gamma_N(k_2), \Rightarrow \gamma_L(k_2) = -\gamma_N(k_2) < 0,$$

where $\gamma_L(k_1)$ includes the external forcing. The energy injected at $k = k_1$, $\gamma_L(k_1) > 0$, is transferred out of the mode $k = k_1$ by nonlinear interaction, $\gamma_N < 0$. At $k = k_2$, the energy transferred to $k = k_2$ nonlinearly, $\gamma_N(k_2) > 0$, is dissipated by viscosity, $\gamma_L(k_2) < 0$. It should be noted that $\gamma_N(k_1) < 0$ and $\gamma_N(k_2) > 0$ do not mean the energy is transferred directly from k_1 to k_2. These inequalities simply represent the instantaneous snapshot of energetics at two wavenumbers.

The energy transfer rates and growth rates can be decomposed in terms of eigenmodes. Using Eq. (13), the fluctuations are written as

$$\xi_{\boldsymbol{k}} = \sum_n \xi_{\boldsymbol{k}}(n), \tag{17}$$

where the mode number n represents the nth eigenmode of the wavenumber $\boldsymbol{k}$. Applying $\bar{\eta}_n^* \bar{\bar{M}}$ in Eq. (12) to Eqs. (4a)–(4c) and multiplying by $\phi_{\boldsymbol{k}}^*(n')$, the energy evolution of the electrostatic potential is represented as follows:

$$\begin{aligned}\frac{\mathrm{d}}{\mathrm{d}t}\mathrm{E}_\phi(\boldsymbol{k},n,n') &= \frac{1}{2}(\tau + k_\perp^2)\frac{\mathrm{d}}{\mathrm{d}t}\mathrm{Re}\{\phi_{\boldsymbol{k}}(n)\phi_{\boldsymbol{k}}^*(n')\} \\ &= \frac{1}{2}\Bigg[\mathrm{Im}\{k_y \epsilon_n p_{\boldsymbol{k}}(n)\phi_{\boldsymbol{k}}^*(n') - k_z k_\perp^2 A_{\boldsymbol{k}}(n)\phi_{\boldsymbol{k}}^*(n')\} \\ &\quad + \mathrm{Re}\left\{\left([\phi,\nabla_\perp^2\phi] - \frac{\beta}{2}[A,\nabla_\perp^2 A]\right)_{\boldsymbol{k},n}\phi_{\boldsymbol{k}}^*(n')\right\}\Bigg] \\ &\quad + (n \leftrightarrow n'),\end{aligned}$$

where $(n \leftrightarrow n')$ represents the term with n and n' switched in the preceding term. This quadratic term depends on both eigenmodes n and n' because the right eigenvectors $\bar{\zeta}_i$ are not orthogonal to each other.

To make matters simpler, the energy equations are grouped into two components of the linearly unstable part and linearly stable part as follows. The fluctuation is split into $\bar{\zeta}_{\boldsymbol{k}}(u)$ of linearly unstable modes (Re $\lambda_i > 0$) and $\bar{\zeta}_{\boldsymbol{k}}(s)$ of linearly stable modes Re $\lambda_i \leq 0$,

$$\bar{\zeta}_{\boldsymbol{k}} = \bar{\zeta}_{\boldsymbol{k}}(u) + \bar{\zeta}_{\boldsymbol{k}}(s), \tag{18}$$

where

$$\bar{\zeta}_{\boldsymbol{k}}(u) = \sum_{\mathrm{Re}\,\lambda_i > 0} a_i \bar{\zeta}_{\boldsymbol{k}}(i), \quad \bar{\zeta}_{\boldsymbol{k}}(s) = \sum_{\mathrm{Re}\,\lambda_i < 0} a_i \bar{\zeta}_{\boldsymbol{k}}(i),$$

and

$$a_i = \bar{\eta}_{\boldsymbol{k}}^*(i)\bar{\bar{M}}\bar{\zeta}_{\boldsymbol{k}} / \bar{\eta}_{\boldsymbol{k}}^*(i)\bar{\bar{M}}\bar{\zeta}_{\boldsymbol{k}}(i).$$

Therefore, the energy equations are

$$\Gamma_{\mathrm{Tuu}}(\xi,\boldsymbol{k}) = \Gamma_{\mathrm{Luu}}(\xi,\boldsymbol{k}) + \Gamma_{\mathrm{Nuu}}(\xi,\boldsymbol{k}), \tag{19a}$$

$$\Gamma_{\mathrm{Tus}}(\xi,\boldsymbol{k}) = \Gamma_{\mathrm{Lus}}(\xi,\boldsymbol{k}) + \Gamma_{\mathrm{Nus}}(\xi,\boldsymbol{k}), \tag{19b}$$

$$\Gamma_{\mathrm{Tss}}(\xi,\boldsymbol{k}) = \Gamma_{\mathrm{Lss}}(\xi,\boldsymbol{k}) + \Gamma_{\mathrm{Nss}}(\xi,\boldsymbol{k}), \tag{19c}$$

where $\xi=(\phi,A,p)$, and the explicit expressions of $\Gamma_{\mathrm{Lnn'}}$ and $\Gamma_{\mathrm{Nnn'}}$ are given in Eqs. (A4)–(A6) of the Appendix. Similar to Eq. (16), the growth rates are defined as

$$\gamma_{ij}(\xi,\boldsymbol{k}) = \frac{\Gamma_{ij}(\xi,\boldsymbol{k})}{2\mathrm{E}_{\boldsymbol{k}}}\gamma_{ij}(\boldsymbol{k}) = \sum_\xi \gamma_{ij}(\xi,\boldsymbol{k}) \quad \text{and}$$

$$\gamma_{ij} = \frac{1}{\mathrm{E}_{\mathrm{tot}}}\sum_{\xi,\boldsymbol{k}} \Gamma_{ij}(\xi,\boldsymbol{k}), \tag{20}$$

where i=T, L, and N, and j=(uu, us, ss). $E_{\boldsymbol{k}}$ is the total energy of the wavenumber $\boldsymbol{k}$.

It should be noted that $\gamma_i(\boldsymbol{k}) = \Sigma_j \gamma_{ij}(\boldsymbol{k})$. The breakdown given by Eqs. (19) and (20) reveals details of the dynamics otherwise not evident. For example, it could address which of the following outcomes might be in force for an unstable mode ($\gamma_{\mathrm{Luu}} > 0$). Assuming the mode is found to lose energy by spectral transfer to other wavenumbers of the unstable eigenmode ($\gamma_{\mathrm{Nuu}} < 0$), the amplitude would be decaying if $\gamma_{\mathrm{Tuu}} < 0$, or its exponential growth would be slowed if $\gamma_{\mathrm{Luu}} > \gamma_{\mathrm{Tuu}} > 0$. The condition $\gamma_{\mathrm{Nss}} > 0$ would indicate energy transfer to stable eigenmodes ($\gamma_{\mathrm{Lss}} < 0$) at the same wavenumber with the condition $\gamma_{\mathrm{Tss}} > 0$ indicating that they grow exponentially. These diagnostics are particularly telling in transient situations such as the onset and evolution of the KHI. However, even in a steady state where $\gamma_{\mathrm{L}} = \gamma_{\mathrm{N}}$, the decomposition into stable and unstable eigenmode components can describe energy branching ratios between these two components.

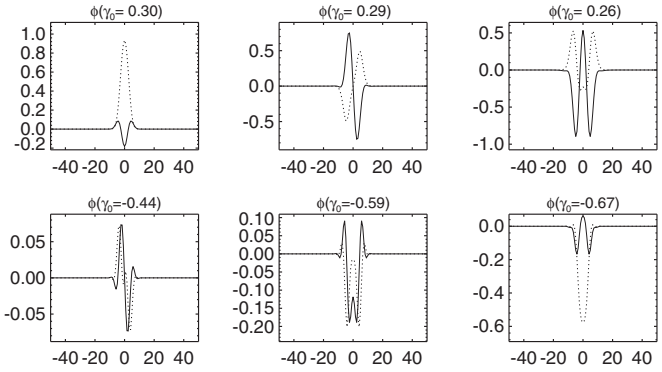

FIG. 1. Radial structures of electrostatic potential ϕ for k_y=0.6. The three unstable modes are plotted in the top panel and the three stable modes, localized in the same region as the unstable modes are shown in the bottom panel. Solid and dotted lines represent the real and imaginary components of the fluctuations.

The energies, energy transfer rates, and growth rates as decomposed in the eigenmode basis include the mixed terms Γ_{us} and γ_{us}. The linear growth rates of unstable and stable modes γ_{Luu} and γ_{Lss} are positive and negative definite, respectively, but the mixed term γ_{Lus} can have either sign. It is important to include this term in analysis and interpretation of results. In this paper, when the stable term γ_{Lss} and mixed term γ_{Lus} have the same sign, these two terms are shown combined as $\gamma_{\mathrm{ss}} + \gamma_{\mathrm{us}}$ for simplicity. If, however, the terms have opposite signs and partially cancel, both terms are shown separately.

IV. NUMERICAL RESULTS

The description of the stable eigenmode is investigated in 2D simulations with $\nabla z = isxk_y$, i.e., $k_z = 0$. The main simulation has a resolution of $(N_x, N_y) = 196 \times 96$, a box size of $(2L_x, L_y) = (100, 20\pi)$, and parameter values $\epsilon_n = 0.3$, $\eta_e = 3.0$, $\beta_e = 0.01$, and $s = 0.2$. This parameter set is relevant because it has a hybrid scenario-like flat q-profile with low magnetic shear.[17]

Figure 1 shows the radial structures of the electrostatic potential of the eigenmodes for $k_y = 0.6$. Each plot is labeled by the linear growth rate γ_0 of the eigenmode. The top three panels are the radial structures of the three most unstable modes and the bottom three panels are stable modes. For the most unstable mode, the electrostatic potential and electron pressure have even symmetry around the resonant point $x = 0$

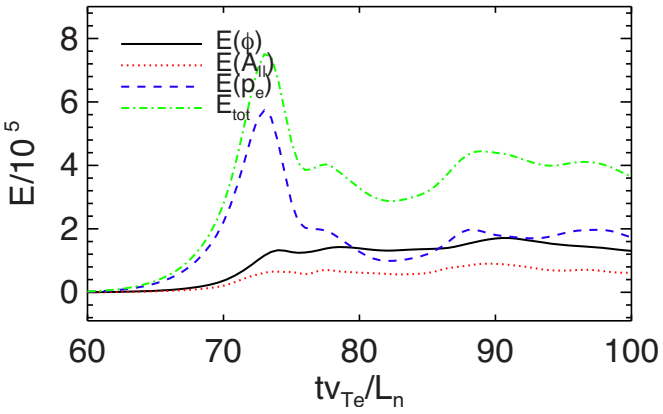

FIG. 2. (Color online) Total energy evolutions (green, dot-dashed) are shown in the linear scale (right) along with the energies E_ϕ (black, solid), E_A (red, dotted), and E_p (blue, dashed) [see Eqs. (7) and (8)].

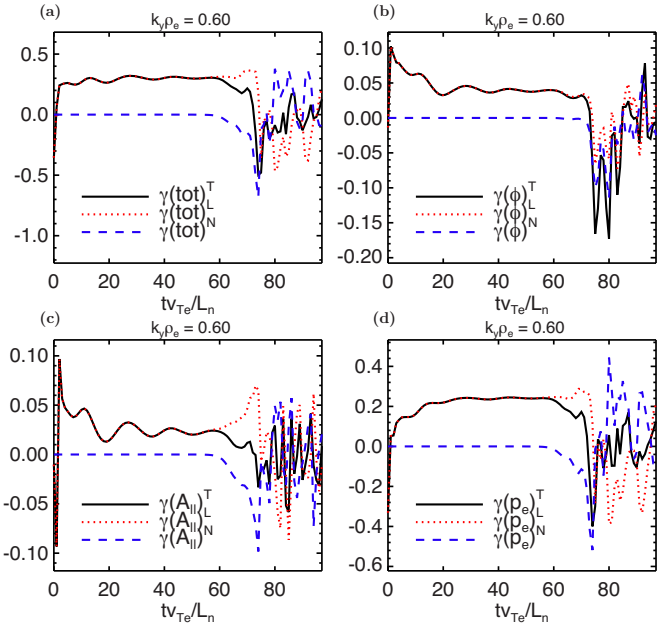

FIG. 3. (Color online) Total, linear, and nonlinear growth rates of γ_T (black, solid), γ_L (red, dotted), and γ_N (blue, dashed) in time: (a) for the total energy, (b) the electrostatic energy, (c) the magnetic energy, and (d) the electron pressure energy [refer to Eq. (16)].

while the magnetic potential has odd symmetry. The width of the electrostatic potential is $\Delta x \sim 20\rho_e$. The second unstable mode has the opposite symmetry. It is noted that the stable modes are localized to the same radial regions as the unstable modes, and hence are expected to play a crucial role in saturation by damping the turbulent energy of the excited unstable modes. The number of the unstable eigenmodes obtained ranges between 5 and 7 for $k_y=0.1-0.9$. These unstable modes trace out the energy evolution dE/dt and the heat flux q_e in the linear phase at each k_y. In practice, the unstable fluctuation of each k_y is calculated from the eigenmode projection and subtracted from the fluctuation of each k_y to obtain the stable fluctuations.

Figure 2 shows the time history of the total energy. It reaches a maximum at $t=73$, starting from randomly initialized fluctuations. As expected, the initial evolution is linear until $t=60$. Nonlinear interaction becomes significant at $t=60$ as evident in Fig. 3. Between $t=60$ and 73, the total energy growth slows down to zero due to nonlinear interaction, and after the peak, the total energy is reduced by 50% and reaches saturation.

The role of KHI is investigated in the current work by examining the evolution with and without the $\boldsymbol{E}\times\boldsymbol{B}$ advection term $[\phi,\nabla_\perp^2\phi]$ of Eq. (4a). This term is conservative, hence removing it does not directly affect energy input or dissipation. It does remove the Kelvin–Helmholtz secondary instability driven by $\boldsymbol{v}_E\cdot\nabla\nabla^2\phi_0$, where ϕ_0 is the amplitude of the unstable mode after it has grown to where the Kelvin–Helmholtz instability condition is satisfied. Moreover, the dynamics without the $\boldsymbol{E}\times\boldsymbol{B}$ convection in Eq. (4a) lacks the spectral transfer of potential energy associated with $[\phi,\nabla_\perp^2\phi]$ and nonlinear cross phase decorrelation. However, because pressure fluctuations are larger than vorticity $\nabla^2\phi$, the decorrelation is supplied by the pressure advection nonlinearity, even when $[\phi,\nabla_\perp^2\phi]$ is removed. Therefore, the primary role of the term $[\phi,\nabla_\perp^2\phi]$ is to produce secondary KHI represented by $\boldsymbol{v}_E\cdot\nabla\nabla^2\phi_0$.

At the most unstable wavenumber $k_y=0.6$, the total growth rates of electrostatic potential $\gamma_T(\phi)$ and electron pressure $\gamma_T(p)$ in the linear phase are seen to be $0.05L_v/v_{Te}$ and $0.2L_n/v_{Te}$ from Fig. 3. We focus on Fig. 3(d), which most clearly shows the effects of KHI. The KHI term is included in the runs of Fig. 3. At $t=60L_n/v_{Te}$, the $\boldsymbol{E}\times\boldsymbol{B}$ advection of electron pressure starts to be effective in transferring instability-driven fluctuation energy to the modes with $k_y\neq 0.6$. Accordingly, the total growth rate of pressure $\gamma_T(p_e)$ is reduced due to the nonlinear energy transfer $\gamma_N(p_e)$, while the linear growth rate remains at the level of the linear stage. At $t=73$, the transition from the linear to the turbulent state occurs, as noted by the onset of rapid variation in growth rates. When the KHI term is not included this transition occurs at a later time, after $t=80$. However, once the transition occurs, there is rapid variation in the growth rates and $\gamma_T(p)\neq\gamma_L(p)$, regardless of whether the KHI term is present or not. This indicates that the KHI enables the transition to turbulence, but the turbulent state, once induced, is largely insensitive to vorticity advection. More will be said about the KHI when Fig. 9 is presented. Pressure advection is clearly a significant player in the nonlinear state. Note that while the pressure growth rates oscillate, the energy injection rate $\gamma_L(k_y=0.6)$ is negative and the nonlinear transfer rate is positive, $\gamma_N(k_y=0.6)\gtrsim 0$. This means that the wavenumber $k_y=0.6$ of maximum instability in the linear phase becomes an energy sink in the nonlinear phase, fed by conservative nonlinear energy transfer. The negative injection rate indicates not just that damped eigenmodes are excited, but that they damp energy faster than the injection of energy by the linear growth rate for the wavenumber at $k_y=0.6$.

A slightly different view of the transition is given in Fig. 4, which shows the eigenmode decomposition of total and linear growth rates. The unstable modes are dominant in the linear phase $t<60$ as expected, as indicated by the similarity of γ_{Tuu} and γ_T for $t<60$. At $t=60$ the growth rate of total energy peaks and turns over as modest damped eigenmode

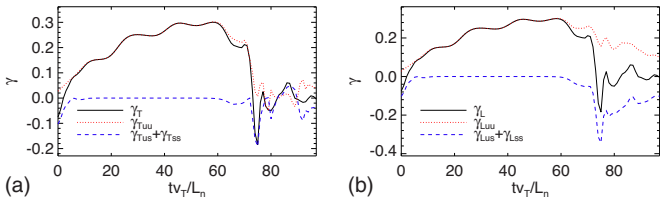

FIG. 4. (Color online) Time evolution of $\gamma_{L,T}$ (solid), $\gamma_{L,Tuu}$ (dotted), and $\gamma_{L,Tus}+\gamma_{L,Tss}$ (dashed) [refer to Eqs. (16) and (20)].

excitation in $\gamma_{Lss}+\gamma_{Lus}$ begins. Stable modes $\gamma_{Tss}>0$ are excited by nonlinear interaction among the eigenmodes at $t>60$ with a rate comparable to γ_{Tuu}. These rates are smaller than the growth rate during the linear phase and oscillate as in Fig. 3. At $t=73$ there is a sharp drop in γ_L and a divergence from γ_{Luu} corresponding to a sharp uptick in the rate of dissipation by damped eigenmodes $(\gamma_{Lss}+\gamma_{Lus})$.

The electrostatic potentials at $t=70$ and $t=76$ are shown in Fig. 5. During the transition, the radially elongated structure of Fig. 5(a), which is the reminiscent of the unstable linear structure, is converted to the vortex-like structures of Fig. 5(b). This transformation is not seen in the simulation without the KHI term. This confirms the presence of KHI in the transition at $t=76$. The significant modification of the radial coherence scale length implicit in Fig. 5 is accompanied by the steep reduction in the heat flux. There is little change in the energy spectrum. Broader radial structures with short radial correlation are indirect evidence of the dissipative structure created by the mixture of unstable and stable eigenmodes in the wavenumbers of the linear instability.

The linear drive γ_{Luu} by unstable modes is the source for turbulent energy. The energy dissipation rate γ_{Lss} by damped modes is negligible in the linear stage ($t<60$) shown in Fig. 4(b). Around $t=60$, the dissipation by damped modes becomes non-negligible and the dissipation becomes critical beyond $t=70$. In the steady and turbulent stage, the linear energy transfer rate of unstable modes is balanced by the linear energy transfer rate of stable modes.

In Figs. 6–8 we examine the wavenumber properties of the energetics for the linear, transition, and nonlinear phases. The linear stage is shown in Fig. 6, which is taken from an average between $t=40$ and $t=60$. The dynamics is dominated by the most unstable modes, which lie between $k_y=0.3-0.8$. At lower and higher k_y, the damped modes are excited significantly. However, from Fig. 4, the total energy dissipation is negligible because the energy of the damped modes is

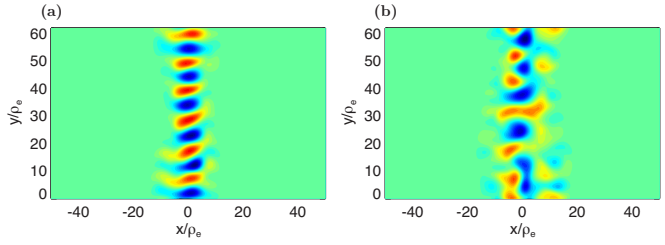

FIG. 5. (Color online) Contours of electrostatic potential (a) at $t=70$ and (b) at $t=73$ after the linear structure is broken by KHI.

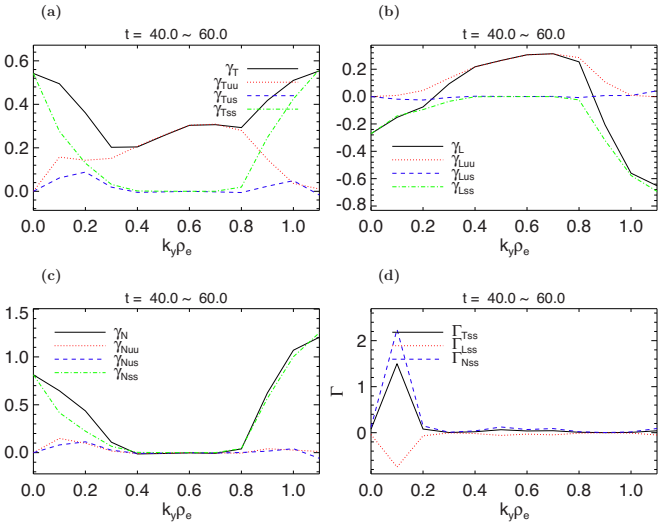

FIG. 6. (Color online) (a) Total growth rate $\gamma_T(k_y)$, (b) linear growth rate $\gamma_L(k_y)$, (c) nonlinear growth rate $\gamma_N(k_y)$, and (d) energy transfer of stable modes at $t=40-60$.

minuscule. A part of the linearly driven energy is nonlinearly transferred to the damped mode at $k_y=0.1$, as inferred from Figs. 6(b) and 6(c). The energy transfer associated with stable modes is shown in Fig. 6(d). Nonlinear transfer dominates at $k_y=0.1$, with 40% of the energy transfer rate dissipated by damped eigenmodes. Still, $\Gamma_{Nss}(0.1)\simeq 2$ is insignificant compared with the linear energy transfer rate at $k_y=0.1$, whose value is $\Gamma_{Luu}\simeq 60$. Consequently, the damped modes play a negligible role in a complete picture of the linear phase, consistent with $\Gamma_{Luu}(0.6)=\Gamma_{Tuu}(0.6)=\Gamma_L=\Gamma_T$.

As we saw in Fig. 4, significant damped eigenmode dissipation occurs in the transition to saturation when total energy growth slows down. The detailed energy analysis is shown in Fig. 7, which depicts the energetics between $t=70-73$. The total energy input into the system is still dominated by unstable modes around $k_y=0.6$. This is evident

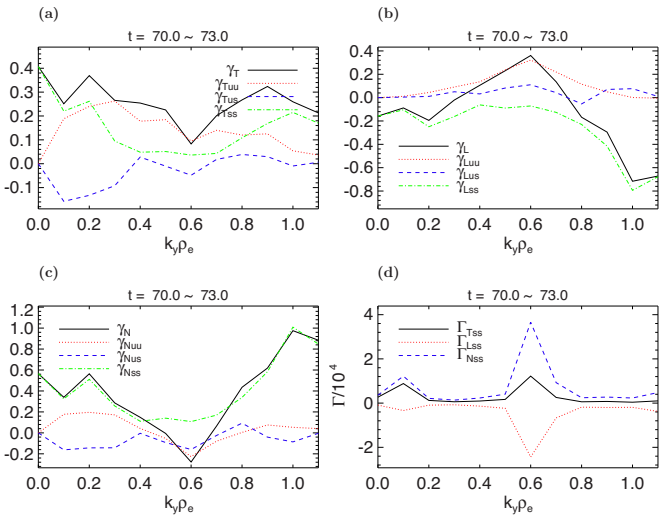

FIG. 7. (Color online) (a) Total growth rate $\gamma_T(k_y)$, (b) linear growth rate $\gamma_L(k_y)$, (c) nonlinear growth rate $\gamma_N(k_y)$, and (d) energy transfer of stable modes at $t=70-73$.

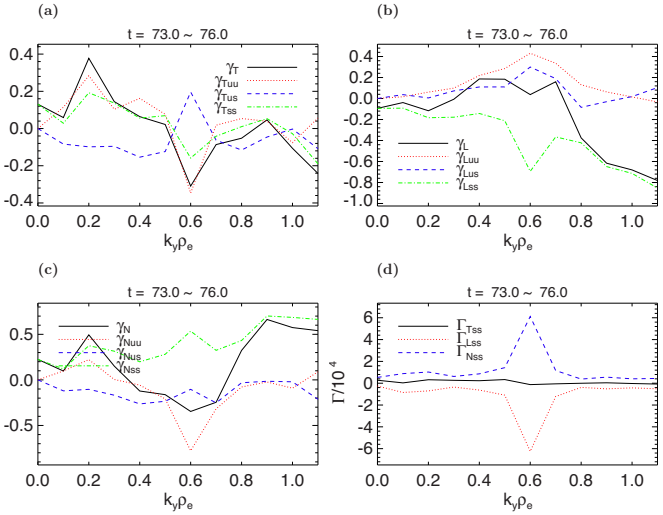

FIG. 8. (Color online) (a) Total growth rate $\gamma_T(k_y)$, (b) linear growth rate $\gamma_L(k_y)$, (c) nonlinear growth rate $\gamma_N(k_y)$, and (d) energy transfer of stable modes at $t=73-76$.

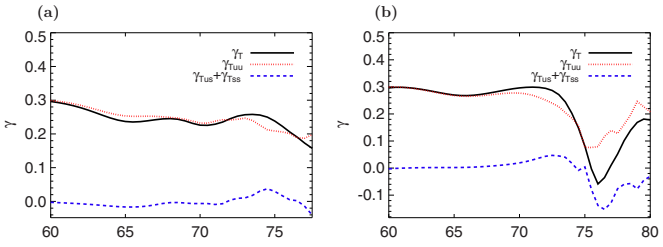

FIG. 9. (Color online) Total growth rates $\gamma_T(k_y)$ without (a) vorticity advection and (b) pressure advection $t>60$. Compare with Fig. 4(a).

from the peak of γ_L at $k_y=0.6$ in Fig. 7(b). The energy input into the system by the linear instability at lower $k_y=0.3$ and higher wavenumbers $k_y=0.8$ is canceled by energy dissipation from damped eigenmodes at the same wavenumbers. Therefore, the wavenumber range of energy injection is narrowed. However, Fig. 7(a) shows that the mode energies of damped and unstable modes are excited over the whole spectrum. From Fig. 7(c) it is seen that there is significant nonlinear energy transfer away from the unstable eigenmode at $k_y=0.6$ and into stable modes at the same wavenumber. Figure 7(d) shows that the energy dissipated by the damped modes at $k_y=0.6$ accounts for 60% of the nonlinearly transferred energy. Net energy input is only 20% of the value predicted by the linear growth rate. Most of the slowdown of total energy growth seen between $t=60$ and 73 is attributed to nonlinear energy transfer to the damped modes. However, that transfer excites the damped eigenmodes and allows them to dissipate some energy. The transfer energy is quantified by γ_N in Fig. 3(a), while the amount dissipated by damped eigenmodes is quantified by the rate $\gamma_{Lss}+\gamma_{Lus}$ in Fig. 4(b).

At $t=73$, the total energy reaches its maximum and decreases rapidly, as noted previously in discussing Fig. 2. The energy decrease is due to nonlinear transfer and dissipation by damped eigenmodes. From Fig. 8 we observe that while the unstable eigenmodes continue to inject energy $\gamma_{Luu}(k_y=0.6)>0$, the injected energy at $k_y=0.6$ is transferred away, $\gamma_{Nuu}>-\gamma_{Luu}$, and the damping rates from stable eigenmodes are as strong as the energy injection rate $\gamma_{Lus}+\gamma_{Lss}\simeq-\gamma_{Luu}$. While the low k_y modes are growing, all the wavenumbers for $k_y>0.4$ are decreasing in Fig. 8(a). All of the energy transferred into stable eigenmodes is dissipated, as seen in Fig. 8(d).

There are two distinct nonlinear processes acting in the saturation of the ETG instability. The first process is fast disruption of the unstable modes associated with the rapid transition of Fig. 4 from the linear state to the nonlinear state with $\gamma_T\approx0$. The second process is related to slow excitation of damped modes, which typifies the steady-state saturated turbulence after the transition. To investigate which nonlinear term in Eqs. (4a)–(4c) is relevant to each nonlinear process, one or the other of the convection terms $\boldsymbol{v}_E\cdot\boldsymbol{\nabla}\nabla^2\phi$ and $\boldsymbol{v}_E\cdot\boldsymbol{\nabla}p$ is turned off at different times in the simulations. When the term $\boldsymbol{v}_E\cdot\boldsymbol{\nabla}\nabla^2\phi$ is turned off at $t<73$, before the energy of the unstable modes reaches the maximum, the rapid transition from the linear to the nonlinear state does not occur. Figure 9(a) shows that the total growth rate of the unstable mode decreases steadily in time toward $\gamma_T\approx0$, but the reduction is not as rapid as it is with the convection. The nonlinear energy transfer from the unstable modes at $k_y=0.6$ to the damped modes is not strong enough to immediately saturate the linearly unstable modes, i.e., $\gamma_{Tuu}>0$, or equivalently $\gamma_{Luu}>-\gamma_{Nuu}>0$ at $k_y=0.6$. The weakening of nonlinear transfer with $\boldsymbol{v}_E\cdot\boldsymbol{\nabla}\nabla^2\phi$ turned off is noted from the value of γ_{Nuu}. When $\boldsymbol{v}_E\cdot\boldsymbol{\nabla}\nabla^2\phi$ is turned off at $t=71$, γ_{Nuu} is lowered by 20% at $t=71.5$.

Weakened nonlinear transfer is also seen in the case where the term $\boldsymbol{v}_E\cdot\boldsymbol{\nabla}\nabla^2\phi$ is turned off at $t=73$, the point in Fig. 4(a), where the energy of the unstable modes starts to decrease, $\Gamma_{Tuu}\lesssim0$. In this case the dissipation rate by the damped modes remains as large as the drive of the unstable modes ($\gamma_{Lss}+\gamma_{Lus}\simeq-\gamma_{Luu}$), and both have similar values to those of Figs. 4 and 8. While these quantities at $t>73$ are as large without the convection as with it, the total growth rate of the unstable modes γ_{Tuu} remains at 0.1 compared to $\gamma_{Tuu}\sim0$ in Fig. 4(a). By inference from $\gamma_{Tuu}=\gamma_{Luu}+\gamma_{Nuu}$, the nonlinear transfer of energy from the unstable modes has become weaker without the convection. Similarly, the nonlinear transfer into damped eigenmodes is also weaker. Because of this weaker transfer, $k_y=0.6$ is still the dominant wavenumber, even after the damped modes assume a prominent role. Even though other wavenumbers are significant in the wavenumber spectrum, the wavenumber $k_y=0.6$ is clearly distinct, an attribute associated with the linear phase.

We can also turn off the $\boldsymbol{E}\times\boldsymbol{B}$ advection of electron pressure $[\phi,p_e]$ at the different times. The results are very different from those in which the $\boldsymbol{E}\times\boldsymbol{B}$ advection of vorticity is turned off. After a transient there is little evidence of a lasting transition. In the transient there is suppression of the unstable mode and large dissipation by damped eigenmodes, as seen in Fig. 9(b). However, after the transient, while the linear rates γ_L, γ_{Luu}, and $\gamma_{Lss}+\gamma_{Lus}$ are similar when the advection of pressure is present, the nonlinear transfer rates are weaker by a factor of 5. Consequently, the damped modes are reduced since the nonlinear energy transfer to damped modes is too weak to compensate the energy dissi-

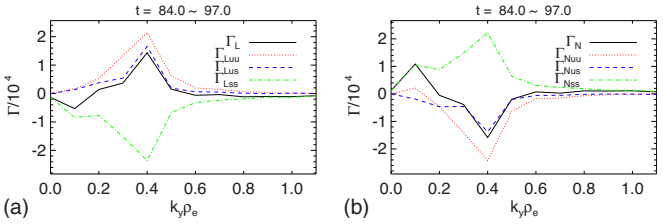

FIG. 10. (Color online) (a) Linear energy transfer rate $\Gamma_L(k_y)$ and (b) nonlinear energy transfer rate $\Gamma_N(k_y)$ at $t=84-97$.

pation by the damped mode, $\gamma_{Lss}<-\gamma_{Nss}<0$ so $\gamma_{Tss}<0$. The suppression of unstable modes disappears within five time units, and the dynamics is governed by the linear growth of the unstable modes. We summarize the results of the numerical experiments that switch on or off the nonlinear terms associated with $\boldsymbol{E}\times\boldsymbol{B}$ convection of vorticity and pressure. $\boldsymbol{E}\times\boldsymbol{B}$ convection of the vorticity is responsible for triggering the transition from the linear phase to a saturated state. It provides a prompt suppression of the instability drive γ_L in which the growth rate of unstable modes is balanced by the dissipation rate of stable modes. This suppression is sustained for long times only by the pressure advection. If $\boldsymbol{E}\times\boldsymbol{B}$ vorticity is artificially suppressed, pressure advection eventually leads to a saturated state, but the approach tends to be more gradual.

By $t=84$ the simulation is close to the saturated steady state. A steady state corresponds to $\gamma_T=\gamma_{Tuu}=\gamma_{Tuu}=\gamma_{Tus}=0$ statistically. Each of these rates is zero by virtue of a balance between energy injection or dissipation and conservative nonlinear transfer. For γ_{Tuu} it is a balance between the growth rate of the unstable modes and nonlinear transfer out of these modes. For $\gamma_{Tus}+\gamma_{Tss}$ it is a balance between nonlinear transfer into damped modes and the dissipation of these modes. From Fig. 10, which shows energy rates in saturation, it is confirmed that in the decompositions of Γ_N and Γ_L into unstable (uu) and stable (ss) components, the unstable and stable components balance to within 10% for $k_y\geq 0.2$. An interesting feature of the saturation is the coincidence of the total linear and nonlinear energy transfer rates with the mixed energy terms above $k_y=0.2$. This feature, i.e., $\Gamma_N\simeq\Gamma_{Nus}$ and $\Gamma_L\simeq\Gamma_{Lus}$, indicates that the linear energy drive Γ_{Luu} and the nonlinear energy transfer Γ_{Nuu} out of the unstable modes are balanced by the linear dissipation Γ_{Lss} and the nonlinear energy transfer to the stable modes Γ_{Nss}, i.e., $\Gamma_{Luu}+\Gamma_{Lss}\simeq 0$ and $\Gamma_{Nuu}+\Gamma_{Nss}\simeq 0$. Along with the conditions of a steady state, $\Gamma_{Tuu}=\Gamma_{Luu}+\Gamma_{Nuu}\simeq 0$ and $\Gamma_{Tss}=\Gamma_{Lss}+\Gamma_{Nss}=0$, the feature suggests that the linear drive by unstable modes is balanced by nonlinear energy transfer, $\Gamma_{Luu}\simeq-\Gamma_{Nuu}>0$, and the energy transferred nonlinearly from the unstable modes to the stable modes is dissipated by the linear dissipation by the stable modes, $-\Gamma_{Nuu}\simeq\Gamma_{Nss}\simeq-\Gamma_{Lss}<0$. This aspect of saturation may prove helpful in analytic work and will be considered further in future work.

The understanding of KHI as a secondary instability of the primary ETG instability requires that the KHI excite the secondary modes with $k_x/k_0<1$ and the poloidal width of the mode $\Delta y/\rho_e\sim k_0\rho_e$, where k_0 is the poloidal wavenumber

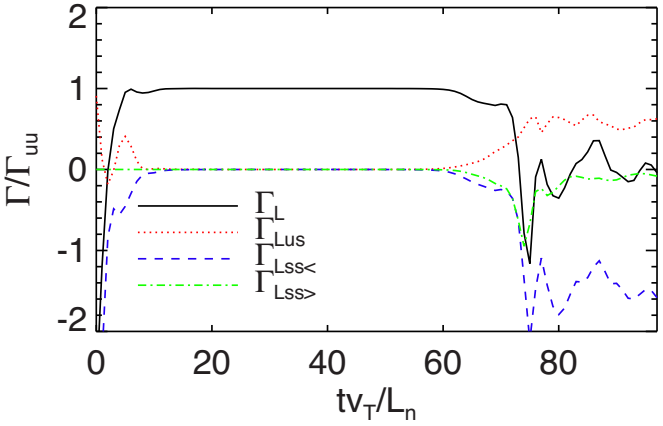

FIG. 11. (Color online) (a) Energy transfer rates Γ_L, Γ_{Lus}, $\Gamma_{Lss<}$, and $\Gamma_{Lss>}$ where the subscripts of <and> represent the sum of the linear energy transfer rate by stable modes over the wavenumbers where there exist unstable modes (low k_y) and where there only exist stable modes (high k_y).

of the most unstable mode.[7] In terms of our analysis, KHI corresponds to a nonlinear energy transfer to wavenumbers of $k_y\rho_e<(k_0\rho_e)^{-1}\simeq 1.6$ from $k_0\rho_e=0.6$, and the formation of small-scale radial structures in electrostatic potential. Therefore, we examine the energy damping by the damped modes according to a division into low and high wavenumbers, k_y.

Figure 11 shows how much of the energy is dissipated at wavenumbers in high and low k_y ranges. $\Gamma_{Lss<}$ and $\Gamma_{Lss>}$ represent the summation of $\Gamma_{Lss}(k_y)$ for $k_y\leq 1.1$ and $k_y>1.1$, respectively, where $k_y=1.1$ is the largest k_y for which an unstable mode exists. The energy transfer rates are normalized by the linear energy input by the unstable modes Γ_{Luu}. In the period leading up to the peak and to saturation, all dissipations are increasing in magnitude. During this time the contributions from low k_y stable modes $\Gamma_{Lss<}$ and the mixed term Γ_{us} cancel one another. At the peak of the energy, the energy dissipation by the stable damped modes increases at both low and high k_y wavenumbers. The momentary increase of the damping at both the low and high k_y wavenumbers is consistent with the narrow poloidal structures of secondary modes in Ref. 7. However, the dissipation by high k_y wavenumbers is significant only during the transition. Even at this time where $\Gamma_{Lss>}$ is at its maximum value, $\Gamma_{Lss<}$ is larger. Thereafter, as the system transitions to the turbulent saturated state, the damped modes at low k_y strongly dominate energy dissipation. The fluctuation energy does not reach very far into the short wavelength range, as evident in Fig. 10. Energy sources and energy dissipation coexist at the same scales.

While the role of the damped modes as a fluctuation energy sink has been emphasized, it is natural to ask about the ratio of damping from the cross-correlation relative to that of the collisional diffusivity terms. Figures 12(a) and 12(b) show energy transfer decomposed into cross-correlation terms (denoted by "C") and diffusive terms (denoted by "D"). These are further broken down into portions associated with unstable and stable modes. In Fig. 12(a) we observe that the diffusive damping of the stable modes behaves as the linear energy transfer rate of the stable mode at high k_y, $\Gamma_{Lss>}$. It is active during the transition but becomes

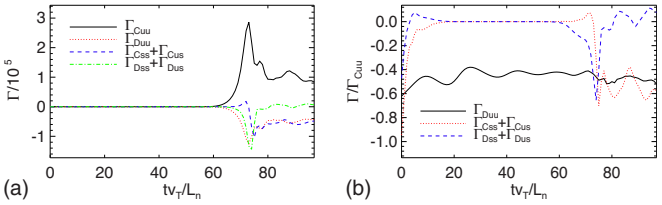

FIG. 12. (Color online) (a) Time evolution of the linear energy transfer rates $\Gamma_L=\Gamma_C+\Gamma_D$, where C and D represent the correlation terms and the viscous terms. (b) Γ_C and Γ_D are normalized by the cross-correlation of unstable modes Γ_{Cuu}.

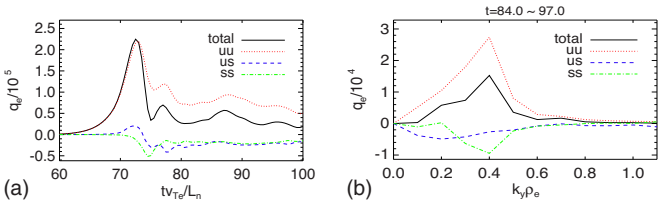

FIG. 13. (Color online) Heat fluxes (a) in time (b) in the wavenumber k_y averaged in the steady state, total and by unstable modes, mixed, stable modes.

low thereafter. In Fig. 12(b), quantities are normalized to the energy transfer of the cross-correlation of unstable modes. The nearly constant trace for the diffusive damping of the unstable modes shows the high degree of temporal correlation with the cross-correlation of unstable modes. It indicates that this damping is the collisional dissipation intrinsic to the instability and therefore tied in some form to instability scales. For long times the cross-correlation of stable modes ($\Gamma_{Css}+\Gamma_{Cus}$) is then seen to be the primary balance for purposes of saturation to the instability (combination of Γ_{Cuu} and Γ_{Duu}). Therefore, the dominant role of the stable mode of low poloidal wavenumber in the energy damping is derived from the cross-correlation, rather than from its diffusive contributions.

The notion of breakup of the primary ETG instability by secondary KHI is useful for obtaining an amplitude threshold for the transition from the linear to the nonlinear state. However, the secondary instability is intrinsically transient. It must saturate at finite amplitude in a transition from its linear behavior, either through tertiary instability (also transient), modification of the electrostatic structure of the primary mode that sustains it, or some other nonlinear effect. As a transient the secondary instability is not a characterization of the time asymptotic nonlinear state. On the other hand, nonlinear energy transfer from the primary mode to other modes over a range of wavenumbers is a complete and persistent process, beginning with the excitation of the secondary mode, and continuing in evolving form into the nonlinear state. When time evolving energy transfer is tracked across stable and unstable modes (with lower growth rates than the most unstable mode), and tagged to the separate nonlinearities of vorticity advection and pressure advection, a more complete picture emerges. Central to this picture is prompt breakup of the primary structure by the transient nonlinear transfer of vorticity advection. This excites large and small scale dissipative structures associated with damped eigenmodes. This is followed by persistent nonlinear energy transfer to large scale damped eigenmodes through the pressure nonlinearity, sustaining the nonlinear state.

The excitation of damped modes generally induces a contribution to transport that is inward, just as unstable modes produce outward transport. Even though the fluctuation energy in the nonlinear simulation is still growing for a long time at the rate of 5% of the linear phase growth rate, there is approximately a steady state for heat flux. Here we describe the heat flux and the fluctuation energy in a steady state with damped modes in play. Assume that there are no mixed energy terms of stable-unstable modes. The energy evolutions are

$$\frac{dE_u}{dt}=(C_u-D_u)+N, \quad \frac{dE_s}{dt}=(C_s-D_s)-N,$$

where the subscripts u,s represent the unstable and stable branches, and C and D are the contributions of the cross-correlation and the diffusive damping as in Fig. 12(a). The nonlinear energy term N is conserved. In a steady state, $C_u=(-C_s)+D_u+D_s$, meaning the energy injected by the cross-correlation of the unstable branch is balanced by the energy sink by the cross-correlation of the stable branch and the viscous damping. Only the correlation part contributes to a heat flux, $Q=C_u+C_s$, where an overall constant is set to one for simplicity. From Fig. 13(a), the total heat flux is 40% of the flux driven by the unstable modes, $Q=C_u+C_s=0.4C_u$. Then the flux driven by the stable modes is $-0.6C_u$. From the energy budget, this means $D_u+D_s\sim D_u\sim 0.4C_u$ time-asymptotically. The mixed terms of stable-unstable complicate this simple analysis. However, as long as $C_{us}+C_{ss}$ is consistent with C_{ss} in sign, we have something approximately represented by $C_u=(-C_s)+D_u+D_s$. The significance of the mixed terms should be further clarified in the future research. Figure 13(b) shows how the electron thermal flux is modified by the damped mode excitation. This damped mode leads to a reduction of the heat flux from its quasilinear estimate by 50% at the dominant wavenumber $k_y=0.4$.

V. CONCLUSIONS

In this paper, we have investigated the role of damped eigenmodes in the transition of the ETG instability from the linear to the nonlinear phase by secondary Kelvin–Helmholtz instability. A 2D electromagnetic ETG fluid model is used in these studies. We confirmed that KHI produces a rapid breakdown of the primary structure. We show for the first time that it creates dissipative structures in low poloidal wavenumber, which persist in the nonlinear phase. High wavenumber structures are only present transiently during the transition.

The standard hydrodynamic picture asserts that the secondary Kelvin–Helmholtz instability drives the energy of the linearly unstable wavenumbers to high wavenumbers where it is dissipated. Numerical calculations show that as much energy is dissipated at low k_y as at high k_y during the transition. The main role of the KHI in the ETG fluid model is to transfer the energy of unstable modes to the high k_y, where it is rapidly dissipated in a transient process, and to low k_y

damped modes, which remain as an energy sink thereafter in the nonlinear phase. The excitation of damped modes at the wavenumbers where unstable modes exist and their energy dissipation are also an essential element of the transition. In the linear phase, the eigenmodes at low k_y are excited by $\boldsymbol{E}\times\boldsymbol{B}$ advection of thermal fluctuation. The low k_y eigenmodes interact with the linearly dominant unstable modes to give rise to the stable modes. The $\boldsymbol{E}\times\boldsymbol{B}$ convection of vorticity, the nonlinear term relevant to KHI, is responsible for initiating the transition from the linear to the nonlinear phase. The subsequent nonlinear phase is sustained by the excitation of damped modes by electron pressure advection.

Analysis using three-dimensional fluid and gyrokinetic simulations will be pursued in the future. Given the involvement of mixed terms in the dynamics linking the energy drive by unstable modes, the nonlinear energy transfer between the stable and unstable modes, and energy dissipation by damped modes, it would be worthwhile to explore theoretical aspects of two-point correlation from the standpoint of eigenmode decomposition. The relevance of pressure advection in the fluid model may point to a process that creates dissipative structures in velocity space in kinetic treatments.

ACKNOWLEDGMENTS

This work is supported by the Department of Energy (Grant No. DE-FG02-89ER53291) and the numerical calculation is done on TACC Ranger with the allocation of Teragrid PHY090009.

APPENDIX: DETAIL EXPRESSIONS OF ENERGY TRANSFER RATES

The expressions $\Gamma_L(\xi,\boldsymbol{k})$ and $\Gamma_N(\xi,\boldsymbol{k})$ in Eq. (15) are given in the following. The linear and nonlinear energy transfer rates for the electrostatic potential fluctuation ϕ are

$$\Gamma_L(\phi,\boldsymbol{k}) = k_y\epsilon_n \,\mathrm{Im}\, p_{\boldsymbol{k}}\phi_{\boldsymbol{k}}^* - k_z k_\perp^2 \,\mathrm{Im}\, A_{\boldsymbol{k}}\phi_{\boldsymbol{k}}^*, \tag{A1a}$$

$$\Gamma_N(\phi,\boldsymbol{k}) = \mathrm{Re}\left\{\left([\phi,\nabla_\perp^2\phi]_{\boldsymbol{k}} - \frac{\beta}{2}[A,\nabla_\perp^2 A]_{\boldsymbol{k}}\right)\phi_{\boldsymbol{k}}^*\right\}. \tag{A1b}$$

The linear and nonlinear energy transfer rates for the parallel magnetic potential fluctuation A are

$$\Gamma_L(A,\boldsymbol{k}) = k_z k_\perp^2 \,\mathrm{Im}\{A_{\boldsymbol{k}}\phi_{\boldsymbol{k}}^* + A_{\boldsymbol{k}}^* p_{\boldsymbol{k}}\}, \tag{A2a}$$

$$\Gamma_N(A,\boldsymbol{k}) = \mathrm{Re}\left\{\left([\phi,\nabla_\perp^2 A]_{\boldsymbol{k}} - \frac{\beta}{2}[A,\phi-p]_{\boldsymbol{k}}\right)(k_\perp^2 A_{\boldsymbol{k}}^*)\right\}. \tag{A2b}$$

The linear and nonlinear energy transfer rates for the electron pressure p fluctuation are

$$\Gamma_L(p,\boldsymbol{k}) = k_y\left\{\frac{1+\eta_e}{\Gamma} - \epsilon_n(1-\tau)\right\}\mathrm{Im}\, p_{\boldsymbol{k}}\phi_{\boldsymbol{k}}^* - k_z k_\perp^2 \,\mathrm{Im}\, A_{\boldsymbol{k}}^* p_{\boldsymbol{k}}, \tag{A3a}$$

$$\Gamma_N(p,\boldsymbol{k}) = -\mathrm{Re}\left\{\left(\frac{[\phi,p]_{\boldsymbol{k}}}{\Gamma} - \frac{\beta}{2}[A,\nabla_\perp^2 A]_{\boldsymbol{k}}\right)p_{\boldsymbol{k}}^*\right\}. \tag{A3b}$$

The energy transfer rates $\Gamma_{Lnn'}(\xi,\boldsymbol{k})$ and $\Gamma_{Nnn'}(\xi,\boldsymbol{k})$ in Eq. (19) are expressed explicitly in the following:

$$\Gamma_{Lnn'}(\phi,\boldsymbol{k}) = c_{nn'}\,\mathrm{Im}\{[k_y\epsilon_n p_{\boldsymbol{k}}(n) - k_z k_\perp^2 A_{\boldsymbol{k}}(n)]\phi_{\boldsymbol{k}}^*(n') + [n\leftrightarrow n']\}, \tag{A4a}$$

$$\Gamma_{Nnn'}(\phi,\boldsymbol{k}) = c_{nn'}\,\mathrm{Re}\left\{\left([\phi,\nabla_\perp^2\phi]_{\boldsymbol{k},n} - \frac{\beta}{2}[A,\nabla_\perp^2 A]_{\boldsymbol{k},n}\right)\phi_{\boldsymbol{k}}^*(n') + (n\leftrightarrow n')\right\}, \tag{A4b}$$

$$\Gamma_{Lnn'}(A,\boldsymbol{k}) = c_{nn'}\,\mathrm{Im}\{[-k_z k_\perp^2\phi_{\boldsymbol{k}}(n)A_{\boldsymbol{k}}^*(n') + k_z k_\perp^2 p_{\mathbf{k}}(n)A_{\mathbf{k}}^*(n')] + [n\leftrightarrow n']\}, \tag{A5a}$$

$$\Gamma_{Nnn'}(A,\boldsymbol{k}) = c_{nn'}\,\mathrm{Re}\left\{\left([\phi,\nabla_\perp^2 A]_{\boldsymbol{k},n} - \frac{\beta}{2}[A,\phi-p]_{\boldsymbol{k},n}\right)\times k_\perp^2 A_{\boldsymbol{k}}^*(n') + (n\leftrightarrow n')\right\}, \tag{A5b}$$

$$\Gamma_{Lnn'}(p,\boldsymbol{k}) = c_{nn'}\,\mathrm{Im}\{[k_y\epsilon_n P_{\boldsymbol{k}}(n)\phi_{\boldsymbol{k}}^*(n') - k_z k_\perp^2 A_{\boldsymbol{k}}(n)\phi_{\boldsymbol{k}}^*(n')] + [n\leftrightarrow n']\}, \tag{A6a}$$

$$\Gamma_{Nnn'}(p,\boldsymbol{k}) = c_{nn'}\,\mathrm{Re}\left\{\left([\phi,\nabla_\perp^2\phi]_{\boldsymbol{k},n} - \frac{\beta}{2}[A,\nabla_\perp^2 A]_{\boldsymbol{k},n}\right)\phi_{\boldsymbol{k}}^*(n') + (n\leftrightarrow n')\right\}, \tag{A6b}$$

where $nn'=(uu,us,ss)$, $c_{uu}=c_{ss}=1/2$, and $c_{us}=1$, and $[\cdot,\cdot]_{\boldsymbol{k},n}$ is the complex amplitudes of the mode $(\boldsymbol{k},n)$ of the Poisson bracket.

[1] D. A. Baver, P. W. Terry, R. Gatto, and E. Fernandez, Phys. Plasmas **9**, 3318 (2002).
[2] R. Gatto, P. W. Terry, and D. A. Baver, Phys. Plasmas **13**, 022306 (2006).
[3] P. W. Terry and R. Gatto, Phys. Plasmas **13**, 062309 (2006).
[4] P. W. Terry, D. A. Baver, and S. Gupta, Phys. Plasmas **13**, 022307 (2006).
[5] D. R. Hatch, P. W. Terry, W. M. Nevins, and W. Dorland, Phys. Plasmas **16**, 022311 (2009).
[6] P. W. Terry, D. A. Baver, and D. R. Hatch, Phys. Plasmas **16**, 122305 (2009).
[7] W. Dorland, F. Jenko, M. Kotschenreuther, and B. N. Rogers, Phys. Rev. Lett. **85**, 5579 (2000).
[8] J. Li and Y. Kishimoto, Phys. Plasmas **11**, 1493 (2004).
[9] F. Jenko, W. Dorland, M. Kotschenreuther, and B. N. Rogers, Phys. Plasmas **7**, 1904 (2000).
[10] B. N. Rogers, W. Dorland, and M. Kotschenreuther, Phys. Rev. Lett. **85**, 5336 (2000).
[11] W. Horton, B. G. Hong, and W. M. Tang, Phys. Fluids **31**, 2971 (1988).
[12] C. Holland and P. H. Diamond, Phys. Plasmas **9**, 3857 (2002).
[13] R. Peyret, *Spectral Methods for Incompressible Viscous Flow*, Applied Mathematical Sciences Vol. 148 (Springer, New York, 2001).
[14] J. J. Dongarra, B. Straughan, and D. W. Walker, Appl. Numer. Math. **22**, 399 (1996).
[15] K. Goto and R. van de Gejin, ACM Trans. Math. Softw. **35**, 1 (2008).
[16] J. P. Boyd, *Chebyshev and Fourier Spectral Methods*, 2nd ed. (Dover, New York, 2001).
[17] E. Asp, J.-H. Kim, W. Horton, L. Porte, E. Fable, and O. Sauter, Phys. Plasmas **15**, 082317 (2008).